

Observation of a deep convection regime with acoustic tomography

Uwe Send and Friedrich Schott

Institut für Meereskunde, Kiel, Germany

Fabienne Gaillard and Yves Desaubies

Laboratoire de Physique des Océans, IFREMER, Plouzané, France

Abstract. In the winter of 1991–1992 a convection experiment was conducted in the western Mediterranean Gulf of Lions, combining a variety of observational techniques. An essential component was an acoustic tomography array, consisting of six moorings, designed to observe the time evolution of the large-scale processes believed to be relevant in a convection regime. Here two-dimensional slice inversions in three directions from the central mooring are used to estimate the volume of convected water and the mean convection depth and to observe the preconditioning and restratification processes before and after the convection. The near-surface layer is well sampled by the acoustics, which show cooling and subsequent entrainment of the warmer Levantine Intermediate Water (LIW) from below, in agreement with mixed-layer calculations. During the 2 months prior to the main convection event the total heat loss of the large-scale field is in approximate agreement with the surface heat fluxes, showing that little net warm-water advection takes place from outside the convection region. The implied confinement of water by the local circulation should be an important factor in setting the location and extent of the deep convection patch. The volume of water modified by convection in this winter is estimated to correspond to an area of order 60 km radius and 1500 m depth. It is argued that the homogenized area implies an annual mean deep water replenishment of 0.3 Sv. The restratification, by the return of less dense water in the surface and LIW layers, occurs first by rapid capping in the near-surface region. Thereafter, the southern and eastern parts of the region restratify in the deeper layers on a 40-day timescale, while a dense core of 50–60 km diameter remains in the northwest until the end of the experiment.

1. Introduction

Deep convection processes in the ocean are believed to represent the main mechanism for the generation and renewal of deep water masses. Thus they are of importance for setting the properties of this water and the subsequent deep transport of quantities like heat, salt, oxygen, or tracers. There are a few locations in the open ocean where deep convection is known to occur with some regularity, such as the Greenland Sea, the northwestern Mediterranean, and the Labrador Sea. Though known for some 20 years [MEDOC Group, 1970], interest in these processes has been renewed in recent years [Schott and Leaman, 1991; Jones and Marshall, 1993; Schott *et al.*, 1994], because of their relevance in climate problems, advances in measurement techniques, and improved modeling capabilities.

Acoustic tomography has the potential to measure the large-scale temperature stratification and heat content, as well as currents and circulation [Munk and Wunsch, 1979]. Thus it is suitable for observing the strong changes in the water column during deep convection events. One such convection experiment had been carried out in the Greenland Sea from 1988 to 1989 [Worcester *et al.*, 1993]. In 1990

a European acoustic tomography group was formed, consisting of the Institut für Meereskunde (IFM) Kiel, Germany, the Institut Français de Recherche pour l'Exploitation de la Mer, (IFREMER) Brest, France and FORTH/IACM Heraklion. With this new tomography capability an experiment (called THETIS) was conceived, aimed at observing simultaneously the different scales known to exist in a convection region such as the northwestern Mediterranean. The result was the mooring array shown in Figure 1, deployed in the winter of 1991–1992. The small scale of individual convection plumes [Schott and Leaman, 1991; Jones and Marshall, 1993] was observed with a mooring triangle of 2 km side-length (A1–A2–T6), equipped with upward/downward looking acoustic Doppler current profiler (ADCP), thermistor strings, and salinity sensors (SEACAT recorders). The large scale, which is the topic of this study, is that of the entire convection patch, i.e., the homogenized region. This scale was addressed with the mooring array T1 through T6, containing mainly the tomography instruments, but also some current meters and temperature sensors. In addition to moored instruments, observations are available from several hydrographic cruises which carried out conductivity-temperature-depth (CTD) work, shipboard ADCP surveys, continuous termosalinograph surface sampling, and Freon tracer work. An introduction of the project is given by the THETIS Group [1994]. Some aspects of the data from the

Copyright 1995 by the American Geophysical Union.

Paper number 94JC03311.
0148-0227/95/94JC-03311\$05.00

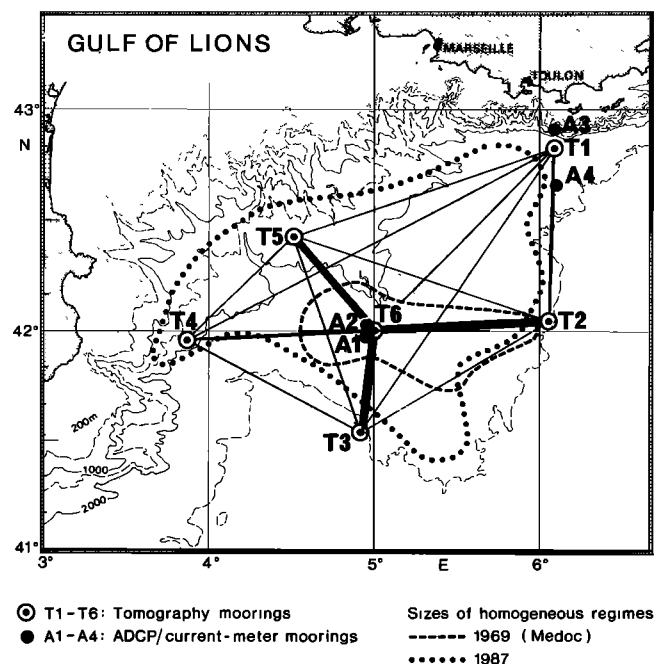


Figure 1. Mooring array deployed during the THETIS experiment, in relation to the convection patches observed in previous years. T1–T6 are the tomography moorings; A1/A2/T6 is the small-scale mooring triangle for high-resolution time series.

experiment are presented and analyzed by Schott *et al.* [1994] and F. Schott *et al.* (Observations of deep convection in the Gulf of Lions, northern Mediterranean, during the winter of 1991/1992, submitted to *Journal of Geophysical Research*, 1995 (hereinafter referred to as Schott *et al.*, submitted manuscript, 1995)) including the current meter and temperature-salinity time series, by Rhein [this issue] using tracer data to infer water mass transformation and movement, and by Mertens [1994] applying a mixed-layer model to simulate the convective mixing.

The purpose of the present paper is the interpretation of the large-scale view of the convection regime provided by the tomography data, taken together with CTD observations, surface heat flux estimates, and mixed-layer simulations. The tomography analysis used here consists of two-dimensional (2-D) slice inversions along radial paths from the center of the convection patch. This provides an overall description of the evolution of the temperature field during the winter 1991–1992, through the various phases of the convection process: cooling, preconditioning, onset of convection, and relaxation toward restratification. We demonstrate that 2-D slices can give valuable and accurate time series of layer-mean heat content averaged over horizontal sections. Quantitative estimates are sought for the size of the homogenized region, for the large-scale heat balance, and for the rate of restratification. A second paper (in preparation) will emphasize the three-dimensional analysis using all tomography instruments available and incorporating other temperature observations (CTD, expandable bathythermograph (XBT), and moorings).

In sections 2 first, the geometry and sampling of the tomography array will be presented. Section 3 gives a short

Table 1. Tomography Instrument Locations

Mooring	Latitude	Longitude	Depth, m	Bottom, m
T1	42° 49.00' N	6° 05.00' E	150	2400
T2	42° 03.20' N	6° 03.07' E	146	2516
T3	41° 32.10' N	4° 55.00' E	154	2530
T4	41° 57.22' N	3° 52.10' E	156	1955
T5	42° 26.03' N	4° 30.73' E	162	1905
T6	42° 00.00' N	5° 00.00' E	150	2200

summary of the data processing and inversion techniques. Section 4 provides an overall description of the temperature field evolution deduced from tomography and compares the large-scale heat content changes with surface heat fluxes. In section 5 the accuracy of the tomography inversions are assessed by comparison with CTD data. The subsections of section 6 analyze the cooling observed in the mixed layer, the horizontal extent and depth of the homogenized regime, and the restratification processes. Section 7 provides the discussion and conclusions.

2. Experiment Geometry and Sampling

The tomography mooring array is shown in Figure 1. The moorings are labeled T1–T6, their positions, depths, and separations are given in Tables 1 and 2. Extensive simulations based on historical data showed that 150 m was an optimal depth in terms of the number of resolvable rays and vertical resolution. The positions were chosen to cover the full extent of the deep-mixed regions that had been observed in previous winter expeditions to the Gulf of Lions (indicated in Figure 1). The extent and shape of the mixed region was to be mapped using radial ray paths from the central mooring T6. Measurements around the perimeter of the whole array, or alternatively around the smaller triangle T2–T5–T3, were also designed to estimate the circulation around the patch. Models indicate that the convective process should result in measurable changes in the circulation but be confined only to a narrow band close to the perimeter of this region [Send and Marshall, 1995]. The circulation analysis will be subject of a later study.

The transceivers were of the Webb Research/Seascan type of 400 Hz frequency, 100 Hz bandwidth, and a source level of 180 dB. Each instrument transmitted 30 or 40 times per day, a transmission consisting of 20 phase shift keying (PSK) sequences of 511 digits. At the frequency of 400 Hz and four carrier cycles per code digit, each transmission thus lasted 102.2 s. The receiving arrays had two channels, separated by half a wavelength, each with a half-wavelength 1-2-2-1 hydrophone arrangement, respectively. For the analyses presented here the two channels were simply averaged in the final lab processing stage (or, in case of one being more

Table 2. Distances Between Instruments

	T2	T3	T4	T5	T6
T1	84.8	171.9	206.1	135.7	127.2
T2		110.5	181.2	133.9	87.3
T3			98.8	105.3	52.1
T4				75.3	93.9
T5					62.8

Distances are in kilometers.

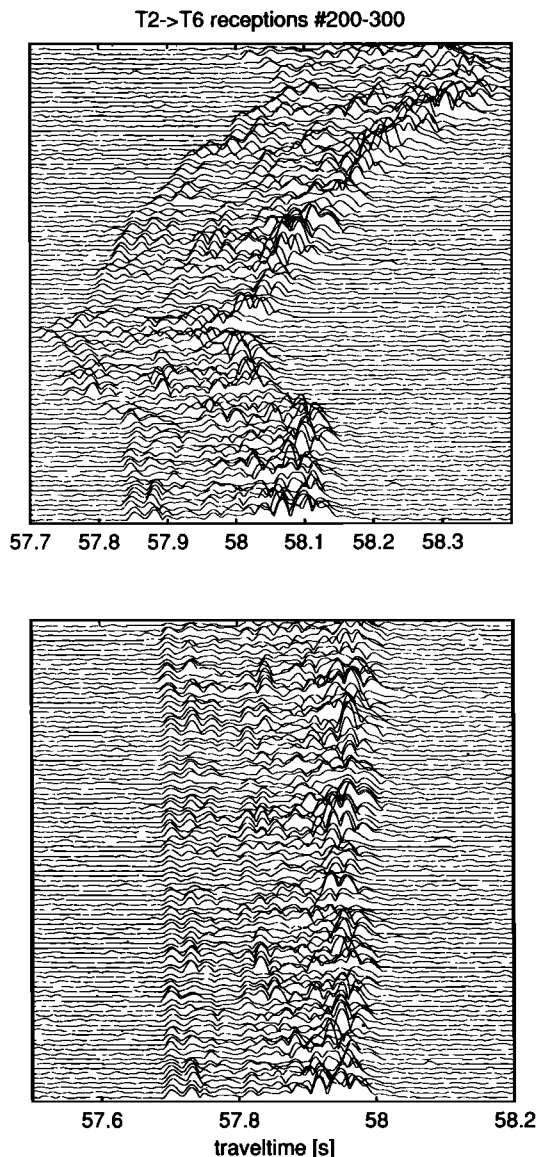


Figure 2. A 5-day sequence of receptions as resulting from the correlation processing to produce the peaks which are identified with individual ray arrivals. The horizontal axis is traveltime in seconds, in the vertical a number of consecutive receptions have been stacked. The top panel shows the raw data, where the meandering of the whole pattern is due to mooring motion. The bottom panel is the corresponding section after mooring motion and clock drift correction.

noisy, only the better one was used). Of the 20 sequences transmitted, 19 were received, starting 2–3 s after the expected first arrival, thus making sure that signals were arriving during the entire sampling period. Demodulation and coherent averaging of the 19 sequences was done inside the instruments. The complex result of this operation, stored on the 200-Mb instrument hard disk, was correlated with the PSK replica during the processing in the lab. Details of the processing can be found in the work by Spindel [1985]. An example of a series of receptions after this processing is shown in Figure 2.

Apart from tomography receptions the systems acquired mooring position data using three bottom mounted acoustic

transponders, plus a pressure measurement, usually before and after each transmission or reception. These allowed relative instrument positioning to within about 1 m. The uncertainty in absolute position mainly comes from the errors in determining the transponder locations (see U. Send et al. (Some developments for acoustic transponder surveys and acoustic navigation, submitted to *Journal of Atmospheric and Oceanic Technology*, 1994) for the procedure used and errors). The absolute instrument positioning depended on Global Positioning System (GPS) accuracy. Water temperature and engineering data (noise, battery voltage, etc.) were also saved regularly in the instruments. A software problem in the controllers led to successive malfunctions of the instruments, and during the February cruise all stations except for T4 were retrieved, repaired, and redeployed. Thus the best spatial coverage is available early in the experiment (mid-December) and starting immediately after the main convective phase (February 18–24). Some instrument pairs, like T6-T3 and T6-T5 yielded rather long time series overall.

3. Data Processing and Inversion

3.1. Peak Tracking and Identification

The correlate data discussed above (and shown in Figure 2) were first corrected approximately for the measured mooring motion by translating the entire arrival pattern of a reception by the time interval $(s - s_{\text{ref}})/c_0$. Here s_{ref} is the reference distance between the mooring pair, s is the actual distance obtained by interpolating the mooring navigation positions onto the reception/transmission times (using distance algorithms for an ellipsoidal Earth), and c_0 is a mean sound speed. A newly developed algorithm for peak tracking and identification was then applied. It determines the identification for a set of observed peaks by minimizing a cost function of the resulting sound speed inversion. The solution (1) requires a sound speed structure consistent with our a priori knowledge of the ocean, (2) minimizes inversion data misfit, and (3) minimizes departure from a smooth evolution of the gravest vertical sound speed empirical orthogonal functions (EOFs). Details can be found in the work by U. Send (Peak tracking by simultaneous inversion, submitted to *Journal of Atmospheric and Oceanic Technology*, 1995). The tracking method also provides an estimate for the accuracy (root-mean-square (rms) traveltime) with which the peaks can be tracked.

After identification and tracking, the rough mooring motion correction is undone, and a more complete correction is applied, using both vertical and horizontal displacements of source and receiver and the ray launch/arrival angles. The results are peak travel times corrected to reference mooring distances and nominal depths, which still contain clock drift. After forming daily averages of the travel times, this clock drift is removed by averaging the reciprocal travel times from transmissions in opposite directions (currents or vorticity may still be analyzed by closing a circuit, where the clock drift also cancels, or by seeking only the vertical shear from relative peak travel times). The result is a time series of daily averages for typically 11–18 peaks, the fluctuations of which are, theoretically, entirely due to sound speed fluctuations of the medium along the ray paths.

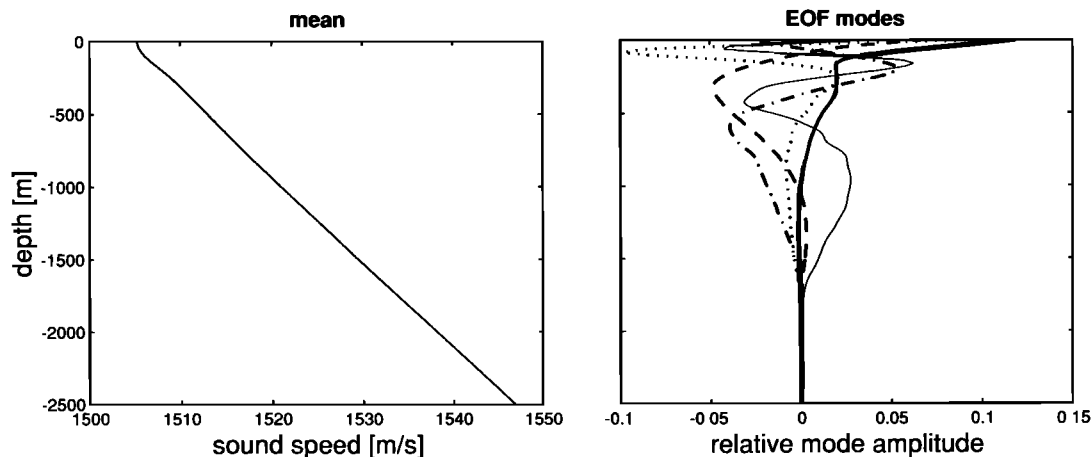


Figure 3. (left) Mean sound speed profile and (right) first five sound speed empirical orthogonal functions (EOFs) $C_i(z)$ resulting from an analysis of the CTD profiles collected during all the cruises of the experiment. Normalization is $\int_{-2500}^0 C_i C_j dz = \delta_{ij}$, the rms sizes of the modes are 17.2, 9.2, 5.6, 4.7, and 3.0 m s^{-1} ; i.e., at depth z the rms sound speed fluctuations due to mode i is $C_i(z)$ times the rms size.

3.2. Inversion

In this study only the horizontally averaged sound speed (or temperature) field is sought, reducing the 2-D section sampled by the sound to a one-dimensional vertical profile at each time. If the sound ray travel times were sensitive to the horizontal variations, the model used to represent the ocean (and to predict the ray travel times) would need to contain a horizontal dimension which would have to be included in the inverse solution. Here the common assumption is made that the observed acoustic travel time fluctuations can be explained largely by the horizontally averaged field [Spiesberger and Worcester, 1983; Spiesberger, 1985]. The small residuals and overall success of the results in this study support this approach. The vertical variability is described by a set of five vertical sound speed modes, derived from an EOF analysis of all the CTD profiles collected during our five cruises. Reasonable care was taken in the EOF analysis to represent approximately equally the typical stratification conditions met in the region: warm or cold surface layer, and strong or weak (absent) Levantine Intermediate Water (LIW) maximum. These first five eigenvectors of the sound speed profile covariance matrix explained 97% of the total variance and are shown in Figure 3. Their root-mean-square amplitudes are listed in the Figure 3 caption. (Availability of a good set of CTD stations from the tomography experiment itself is not necessary for this study. Initially, the data had been inverted with EOFs derived entirely from historical data, and the layer-average temperatures obtained below differ only insignificantly. However, since we want to do the best analysis possible with all the data available, the CTD EOFs from the experiment itself were preferred.)

Reference ray traces were carried out through the mean sound speed field shown in Figure 3 for each mooring pair, using the reference distances and nominal depths respectively. Then, keeping the ray paths fixed, the effect of each EOF mode on each ray travel time was calculated by integrating the perturbation travel time along the paths. This yields the observation matrix \mathbf{G} , which connects the sound speed EOF amplitudes \mathbf{m} and the travel time perturbations \mathbf{d} by the linear relation $\mathbf{G}\mathbf{m} + \mathbf{e} = \mathbf{d}$, where an observational error \mathbf{e} has already been added (uppercase boldface letters

denote matrices, lowercase boldface letters represent column vectors). The inverse estimate (denoted by a circumflex) employs the stochastic inverse, also called the Gauss-Markov estimate [e.g. Aki and Richards, 1980]

$$\hat{\mathbf{m}} = \mathbf{W}\mathbf{G}^T[\mathbf{G}\mathbf{W}\mathbf{G}^T + \mathbf{E}]^{-1}\mathbf{d} = \mathbf{G}^{-g}\mathbf{d} \quad (1)$$

Here the covariance matrices for the mode amplitudes \mathbf{W} and the errors \mathbf{E} are taken to be diagonal (containing only the EOF or error variances), and the observational error was taken to be 3–5 ms for the various ray arrivals, based on the tracking skill. Inverted sound speed profiles were converted to potential temperatures using the relation $\theta' = c'/3.35$, where θ' and c' are the potential temperature (in degrees Celsius) and sound speed deviations (in meters per second) from a perfectly mixed water column with the deep water properties $\theta = 12.78^\circ\text{C}$. (This is a tight relation in this region at all depths. Using all CTD stations from all cruises as a test, the rms error in predicting θ from the sound speed with this formula is 0.02°C .) For each mooring pair the exact distance needs to be known to within a few meters for useful temperature inversions. As explained above, relative motion is tracked by the mooring motion system, but a single unknown constant (mean distance) remains. This has been determined by matching the inversions with the CTD data used to initialize or to check the inverse calculations (see also below).

4. General Evolution of the Regime

Plate 1 shows the tomography inversion for range-average potential temperature between the mooring pair T6-T3 as a function of depth and time during the experiment. The most prominent feature of the panel is the subsurface temperature maximum of the LIW, a warm and salty water mass originating in the eastern Mediterranean. This property of the stratification is well sampled by the tomography and will be of important use later on.

The surface layer is another region of interest. It is seen to be warm at the beginning of the experiment and is cooled as time progresses into the winter season. After some fluctuations this layer attains a minimum temperature in late

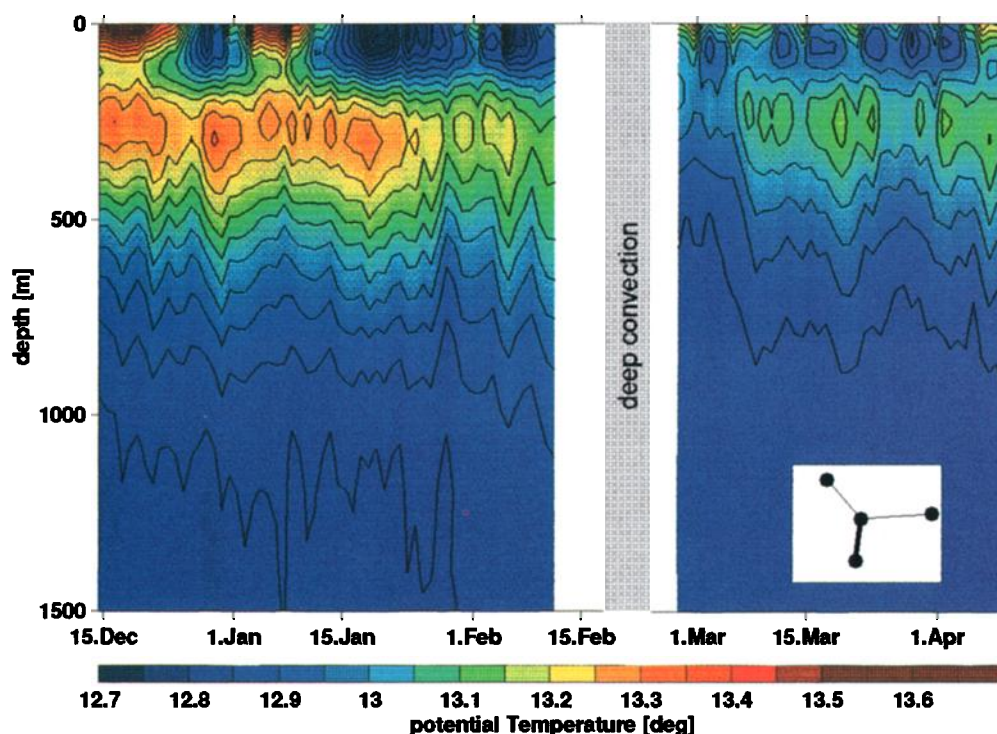


Plate 1. Color contour plot of the depth and time evolution of the range-averaged potential temperature (T6-T3) derived from the tomography data. Contour interval is 0.05°C .

January, after which it becomes dense enough to mix with the warm LIW below. Before this the LIW is present all the time, but from January until mid-February, the amplitude of the temperature maximum is continually reduced, apparently by the cooling and mixing from above.

During the tomography data gap at the end of February the main deep convection activity occurred. Fortunately, we have good shipboard and moored observations during this period. Our CTD data show maximum convection depths of 1700 m. The tomography network was operational again a few days later and clearly shows the cold water from top to bottom after the convection (Plate 1). After this, water of different temperatures reappears in the surface layer more or less immediately, while the warm LIW seems to return only very gradually (and not completely) over the course of the experiment.

The tomography inversion shown in Plate 1 is meant to document the overall evolution and sequence of events during the winter 1991–1992 and to exemplify the results available from the tomography. There are other observations, both moored [see *THETIS Group*, 1994; *Schott et al.*, 1994, also submitted manuscript, 1994] and shipboard CTD surveys, which support and complement the features shown in Plate 1. A number of those observations will be used in the following sections to complete the picture and help the interpretation of the tomography data.

It is worthwhile to compare the horizontally averaged heat content of the water column derived from the tomography with the integral of the estimated surface heat fluxes. The main source for continuous time series of heat fluxes during our experiment was the high-resolution Peridot model for the Mediterranean of the French Meteorological Office. It provides all the flux terms averaged over 12-hour intervals.

Ship-based observations in the region revealed that the model terms had some obvious biases, which were also found in the basin-wide Peridot comparison study of *Martel and Martel* [1994]. Appendix A gives the details of corrections applied. Overall, the surface heat flux thus determined is believed to be accurate to about 20 W m^{-2} . Figure 4 shows the 0–1500 m heat content from the T6-T3 and T6-T5 tomography inversions together with the integrated (corrected) Peridot flux. (The T6-T3 rays did not sample depths below about 1000 m, thus information below this depth is extrapolated using the a priori knowledge contained in the EOFs. Later it will be shown that this seems to work. In Figure 4a however, we also include the 0–1000 m heat content, which shows very similar agreement with the heat flux integral.) The flux integral was initialized with the heat content of a central CTD station from early December. The uncertainty interval resulting from a systematic heat flux error of $\pm 20 \text{ W m}^{-2}$ has been indicated in Figure 4 as well.

In general, the heat content follows the heat flux integral for the whole period of the experiment. During the seasonal cooling phase leading up to the convection there are some warm advective events visible (early January and early February), especially for the pair T6-T3. These events are shown below to result from the more stratified water meandering on and off the T6-T3 line. These cause temporary deviations of the range-average heat content from the heat flux integral. The heat content right after the convection (when the stratified region has moved off of T6-T3 again) is in good agreement with the total heat flux integral. This means that in spite of temporary movement of surrounding warmer water in and out of the region, little net advection from outside has occurred during the cooling period shown. To check the validity, this statement in view of the uncer-

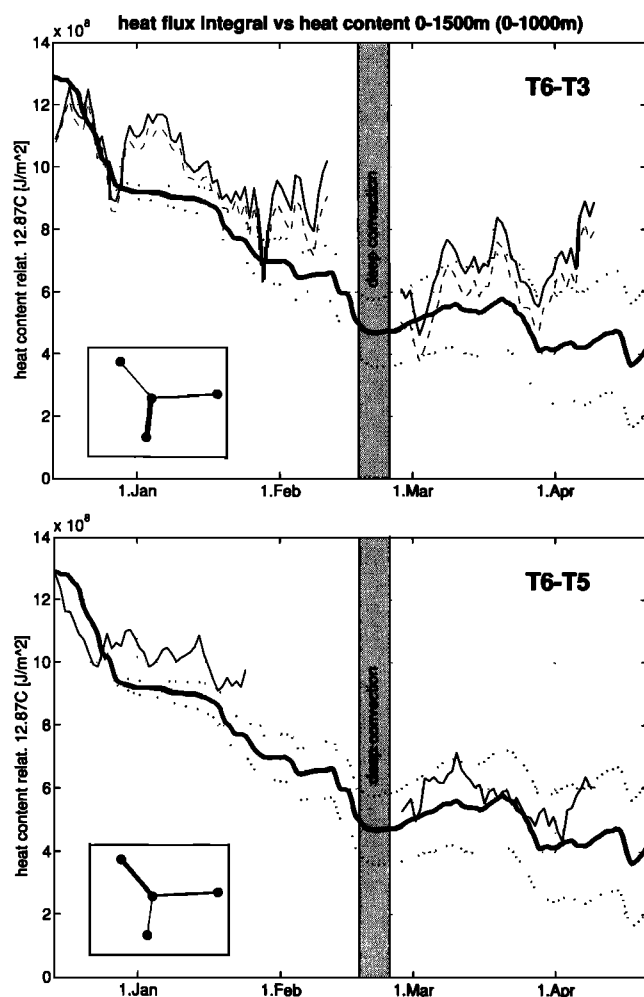


Figure 4. Heat content relative 12.87°C of the 0–1500 m layer (thin line) from the tomography inversions (dashed line: 0–1000 m), compared with the time integral (thick line) of the surface heat flux provided by the Peridot model for the center of the moored array. The heat flux integral has been initialized by a CTD profile from the center of the array. The dotted line indicates the estimated uncertainty arising from a maximum systematic error of $\pm 20 \text{ W m}^{-2}$ in the heat flux.

tainty of the heat flux (dotted lines in Figure 4), it should be verified that a potential exchange of surrounding water would have created a warming greater than this uncertainty. Inspection of our CTD surveys shows that in the immediate surroundings of the convection region, the stratified upper 500 m of the water column have a $2 \times 10^8 \text{ J m}^{-2}$ larger heat content than within this region all the time. Any significant permanent horizontal exchange on the 2-month timescale considered would thus cause a deviation from the heat-flux integral at the time of convection which is larger than the uncertainty shown in Figure 4. We can therefore conclude that the stratified water which needs to be eroded by the cooling inside the convection region has a residence time of at least the 2 months which are necessary to reach the deep convection.

After the convection event, advective warming relative to the heat flux integral can be seen. The rather weak warming at T6-T5 will be shown later to be due to rapid advection in the near-surface layer. At T6-T3, postconvection warming

events appear qualitatively similar to the advective events in January and February. However, estimates for individual vertical layers (see Figure 6), instead of the vertical integral shown here, reveal that the nature of the warming in March and April is rather different, consisting of a well-defined restratification at the LIW level (see also section 6).

5. Tomography Versus CTD Data

CTD data provide vertical profiles with high resolution and accuracy at a number of discrete points in space and during a few time periods, while tomography inversions yield continuous sampling of horizontal averages with less vertical resolution. Comparison of these types of data illustrates their complementary nature while at the same time providing a test for the tomography data themselves.

Figure 5 shows inversions for a seasonal sequence of range-average temperature profiles from tomography, for times at which there were several CTD profiles available at or between the moorings used. The individual CTD profiles are plotted together with the corresponding inversion. The tomography inversions generally are in good agreement with the CTD profiles, in the sense that they represent smoothed profiles which pass through the range of observed CTD values at each depth, to within the error bars of the inversion. This inversion error estimate is indicated in one of the plots (later it will be shown that for layer averages, the error is much reduced). High spatial variability is seen in the CTD profiles along the selected paths after the onset convection. This makes it difficult to assess the distribution of properties, even along a single section, from CTD data. The expectation is that the tomography inversions provide a range average over the vertical structure present. This cannot be rigorously proven since two or three CTD profiles do not necessarily provide a good range average and also since the type of presentation in Figure 5 is not suited for quantitative checks (see also Figure 6). However, the comparison of profiles shows that the inversions do pass through the ensemble of the individual CTD stations. Also, the error bars shown for one of the inverses document that frequently the spatial variability is larger than the inversion error even at individual depths.

A more useful and quantitative way to compare the tomography inversions with CTD data is shown in Figure 6. In the figure, averages have been formed over three depth intervals of interest, the surface layer (0–150 m), the LIW layer (150–500 m), and the whole upper 1000 m. The error limits (see Appendix B) are much smaller now, since the acoustic sampling provides a more accurate estimate of layer averages than of values at a specific depth. For comparison now the layer averages of the (range average) temperatures have also been estimated from hydrography for the times where at least two CTD stations were available at or between the mooring pair used for the inversion. These quantities are included in the figure as circles. The agreement is good at all stages of the evolution, and especially so for the deep layer where small-scale near-surface or LIW variability (which may be missed by the CTD sampling) contributes relatively less. All the mooring pairs processed so far show a similar agreement. Note that only a single constant has been adjusted for all layers and all times, to optimize the agreement, corresponding to the unknown absolute distance between the moorings (to the required

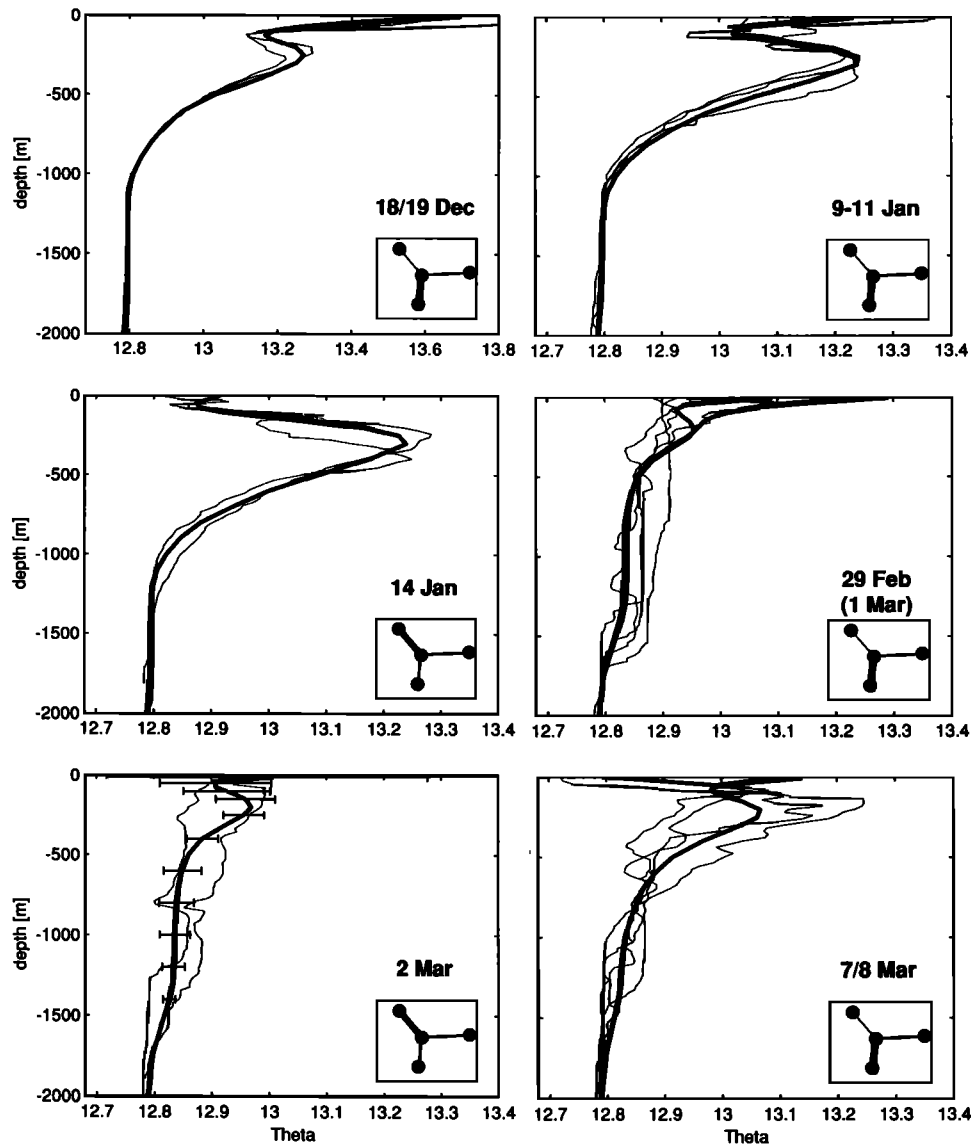


Figure 5. Examples of range-averaged inverted potential temperature profiles from the tomography observations (heavy line), compared to individual CTD profiles at/between the corresponding moorings (thin line) at the time of the tomography data used. The plot for March 2 also includes an estimate for the inversion errors, as explained in the text.

accuracy of a few meters). The type of data shown in Figure 6 forms the main basis for quantitative studies concerning the convection regime, and the above comparison documents the accuracy of those results.

6. Processes in the Convection Regime

6.1. Mixed-Layer Cooling

Since the acoustic propagation during this winter season is surface reflected, the tomographic observations have the advantage of sampling the entire upper layer, from approximately the instrument depths (150 m) upward. Thus they provide a good average of the surface-layer temperature, in addition to averaging horizontally, between two moorings. This makes them a good complement to moored temperature observations, which are taken at a point and which (for subsurface moorings such as employed in our study) extend

only from 50 or 90 m downward. Figures 7a and 7b show the 0–150 m range average temperature from tomography for the mooring pairs T6-T3 and T6-T5, compared to the same quantity from a simple mixed-layer model calculation (C. Mertens, personal communication, 1994). The latter is a simple one-dimensional Krauss-Turner type model which was initialized with a CTD profile taken there in December and which was driven by the (corrected) heat fluxes and winds from the Peridot model output at a grid point near T6. Also included in Figure 7 are temperatures at the moorings T6 (center) and T3 (south). After the convection, no mooring time series is shown, since for that period only data from 150 m downward are available.

The initial cooling observed in the tomography and point measurements is well explained by the surface fluxes which drive the mixed-layer calculation. After about 20 days a strong warming event is observed in the range average to the

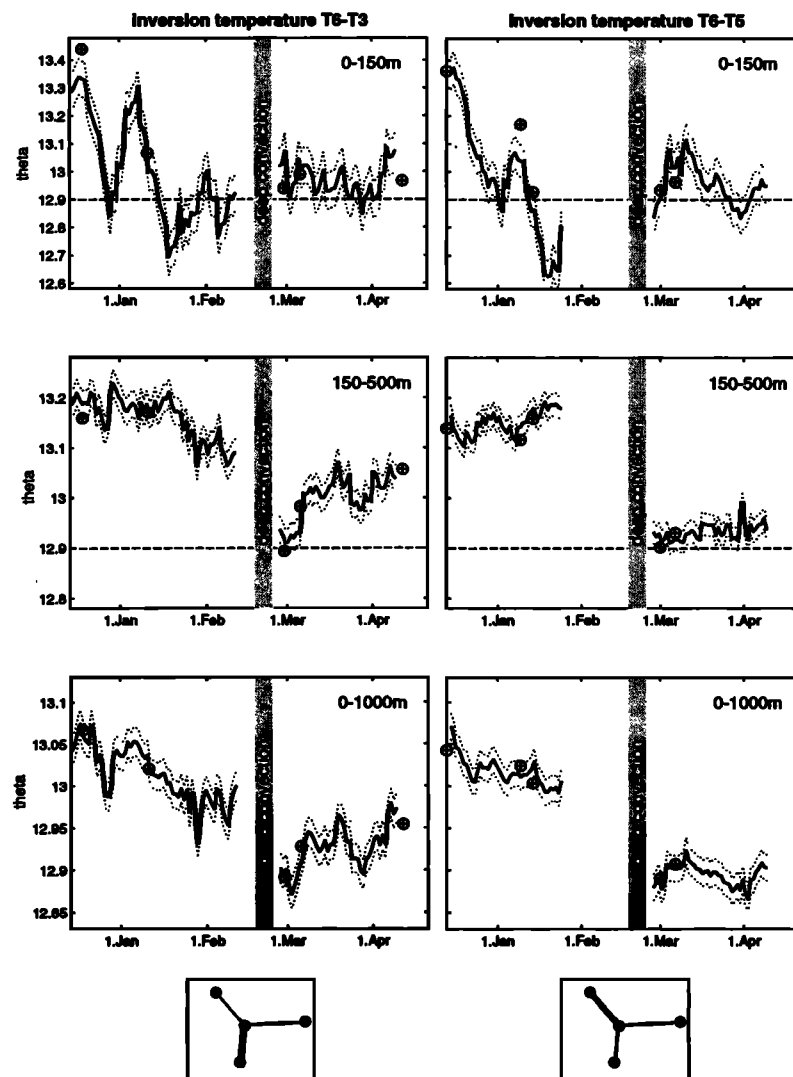


Figure 6. Time series of range-averaged potential temperatures for (left) T6-T3 and (right) T6-T5, averaged over the layers (top) 0–150 m, (middle) 150–500 m, (bottom) 0–1000 m. For comparison, the same layer averages have been formed for CTD stations between the mooring pairs when available, and are plotted as circles. The rms error estimates are indicated as dotted lines about the inversion time series. The dashed line at 12.9°C gives the temperature values found during ongoing active convection.

south (Figure 7a). This is due to warm water moving temporarily into the southern half of the mooring array, as shown by the local temperatures at the moorings (Figure 7a): The (90 m) temperature at the southern mooring T3 shows clearly that this location is close to the boundary between the colder preconditioned water and the warmer surroundings, since this front moves in and out repeatedly past the T3 sensor. During the large peak in the range average the warm water had covered T3 and appears to have reached partially to the central mooring (small temperature increase at T6 and in the T6-T5 average). By mid-January this warm water has mostly receded again.

Around January 15–20, the coldest surface-layer temperatures are reached, which makes the water dense enough to mix with the warmer LIW below. This causes a warming of the surface layer, in spite of continued cooling. The timing of this event predicted by the mixed-layer model agrees well with the tomography inverses, and better than with the mooring time series. The minimum temperature reached in

the T6-T3 inverse is reasonably reproduced by the model, while at T6-T5 colder water is observed than predicted. Trials with different initial CTD profiles for the mixed-layer runs have shown, however, that such low temperatures are possible depending on the initial stratification.

After the onset of LIW entrainment the tomography measurements of the surface layer warming and of the LIW cooling are in approximate agreement with the mixed-layer calculation (Figures 7a and 7c). The small mismatch in the range averages during this phase results from the warm water boundary having moved into the array slightly past the T3 mooring, resulting in absence of LIW entrainment at that point. However, this water apparently occupies only a small fraction of the T6-T3 path since the deviation from the model in the range average is only small. Starting in early February, a large departure between prediction and observation is seen in the LIW layer (Figure 7c), which must be due to more pronounced advection in the southern region. Only half of the expected LIW cooling is observed, indicating that then

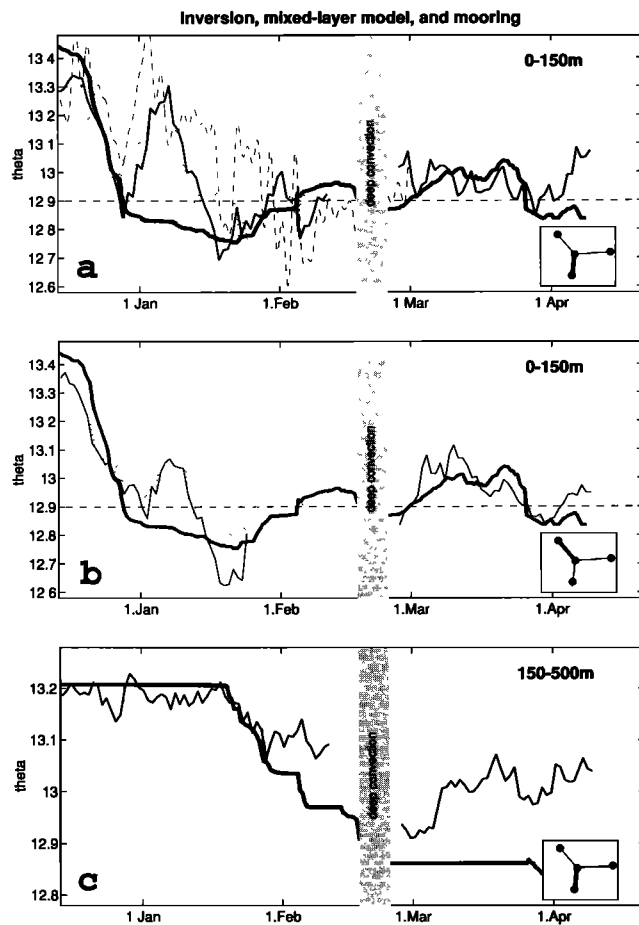


Figure 7. Tomography inverse (solid thin line) for 0–150 m layer temperature at (a) T6–T3 and (b) T6–T5, compared to a mixed-layer simulation (solid thick line), see text. (c) Same as Figure 7a, but for 150–500 m layer between T6 and T3. Also included are mooring time series of the 50–150 m mean temperature from several sensors at mooring T6 (light-dotted line) and the 90 m temperature at mooring T3 (light-dashed line).

only half of the T6–T3 path was covered with water where the LIW stratification was eroded. This condition seems to have persisted until the deep convection phase: our CTD observations of that phase (see below) show that only a smaller part of the distance from T6 to T3 was mixed deep in the first days after convection. During the end of February and the first days of March, however, both in situ and tomography data show mixed water along most of T6–T3. Thus even after convection the southern limit of the array is a place, where the front between stratified and unstratified water moves in and out of the array repeatedly.

6.2. Deep Convection Volume

Inspection of the CTD profiles during and after the main deep convection event shows that there is a clear distinction between stations showing convection and those that do not. Figure 8a and 8b show all the CTD profiles classified according to the simple criterion of whether $\max(\theta_2) < 12.98^\circ$, where θ_2 are the potential temperatures of the LIW layer 150–500 m (layer 2 of the inversion plots). Those stations with higher temperatures in that layer (Figure 8a)

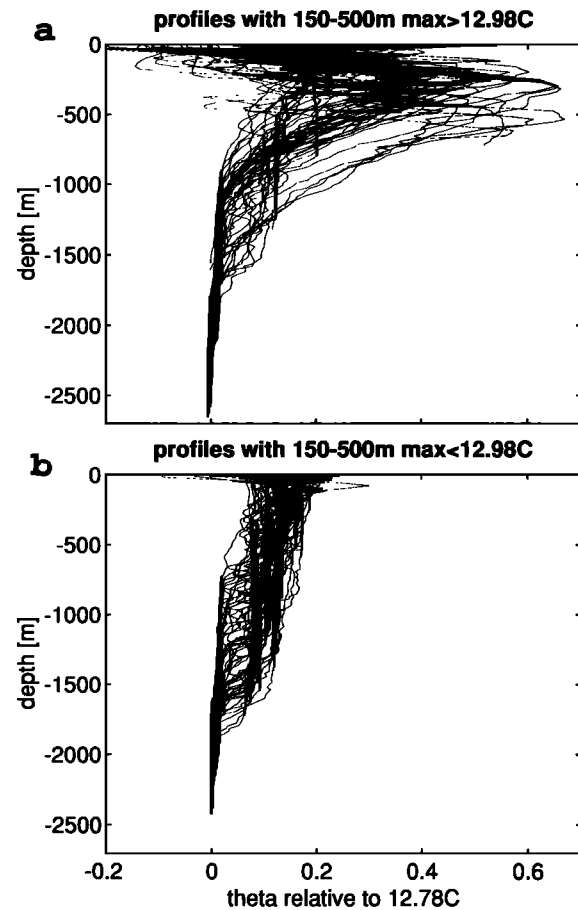


Figure 8. Plot of *Poseidon* CTD profiles: (a) sorted profiles showing stratified characteristics, (b) remaining profiles with convection characteristics. The sorting criterion is explained in the text.

clearly show the typical maximum of the LIW, while the other ones (Figure 8b) are typical convection profiles with a nearly constant temperature profile down to the local convection depth.

This strong distinction in the LIW layer allows use of the tomography data to estimate the area occupied by convected water as follows. Assuming that there can only be water of the convection temperature θ_{conv} and of the stratified temperature θ_{LIW} in this layer, the tomography range average is $\bar{\theta} = c\theta_{\text{conv}} + (1 - c)\theta_{\text{LIW}}$, c being the fraction of well-mixed water. Choosing $\theta_{\text{conv}} = 12.91^\circ \pm .03^\circ$ from all the convected profiles in Figure 8, and θ_{LIW} at the local preconvection values, the tomography data yield c . The accuracy should be 10–20%, resulting from the 0.03° uncertainty in both θ_{conv} and θ_{LIW} .

This calculation has been performed in the three main radial directions from the central mooring T6, i.e., for pairs T6–T3, T6–T2, T6–T5. The result is shown in Figure 9, which plots the fraction of stratified water along each path. After the main convection event, about 100% of the path T6–T3 and T6–T5 are occupied by convected water. Only 70% of the T6–T2 distance is covered with convection. These results are consistent with CTD observations obtained during the cruise which coincided with the convection activity. Assuming an idealized circular geometry for the convection patch,

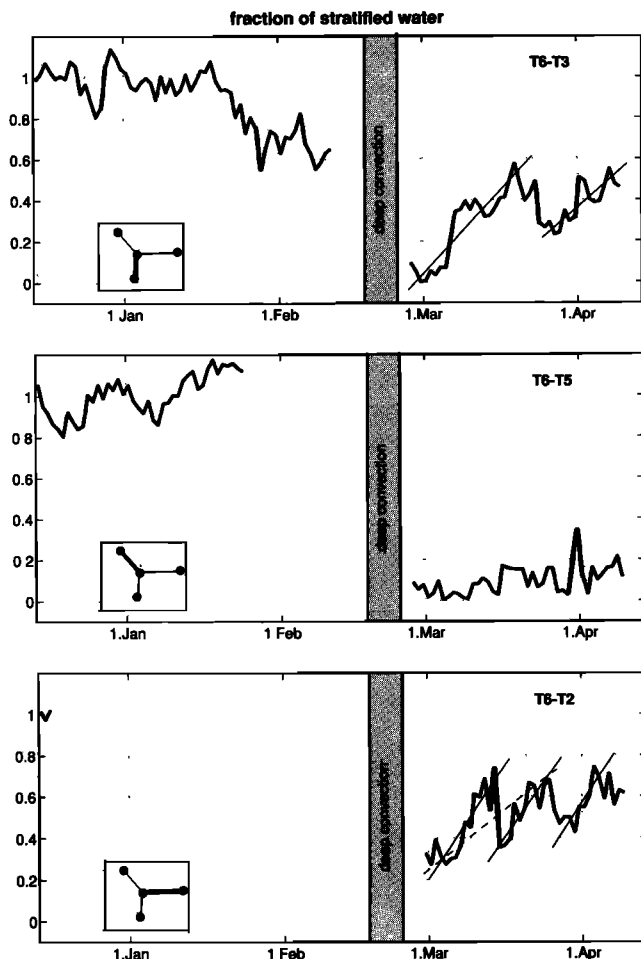


Figure 9. Estimate of the fraction of stratified water along the three paths from the central mooring ((top) T6-T3, (middle) T6-T5, (bottom) T6-T2), using the range-average temperature in the LIW (150–500 m) level (see text). The thin straight lines are estimates of the warming rate during the restratification, the dashed line is the rate including the one cooling event which appears to be due to meandering (see text).

its size can then be estimated with the above information. The patch extends 70% from T6 to T2 (to the east), in the south it extends approximately to T3 (the front has moved in and out at T3, so it cannot extend much beyond T3), and in the north it includes T5 (but cannot reach much beyond T5, because of the coastal current and the topography shoaling to less than 1500 m within 15 km of T5). This results in a circle of approximately 60 km radius.

Following *Send and Marshall* [1994], the deep water formation rate can be estimated from this homogenized area A as follows: The convection has created a volume of dense water from the surface at least to middepth. Assuming that the climatological level of the deep water (DW) is the layer below depth H_{DW} , the additional volume of dense water now present is the part of the homogenized column above H_{DW} ; i.e., $A \times H_{DW}$. If one assumes that this dense water eventually settles down into the deepwater pool, the new volume added to the pool is given by $A \times H_{DW}$. This is different from the volume of water affected or modified by convection, e.g., enhanced with tracers. The latter estimate

includes the whole water volume mixed by the convection, i.e., $A \times h_{conv}$, where h_{conv} now is the area-average convection depth which will be estimated below. Taking $A = \pi (60 \text{ km})^2$ from above and $H_{DW} = 1000 \text{ m}$ (using the tracer signature for the deep water in the work by *Rhein* [this issue]), a deep water formation rate of $A \times H_{DW} = 1.1 \times 10^{13} \text{ m}^3$ per year, or approximately 0.3 Sv, results from this one event. This number is in approximate agreement with the observed outflow of deep water at Gibraltar [*Bryden and Stommel*, 1982; *Bryden and Kinder*, 1991].

6.3. Convection Depth

The tomography inversions apparently also can provide approximate depths of the convective layer. This is somewhat of a surprise for two reasons. First, the vertical modes used for the inversions are smooth functions, especially at depth, and are unable to produce the steps resulting in the temperature profile due to convection. Second, for the shorter mooring distances the sound rays are not deep enough to sample the whole depth down to 1500 m (which was observed with the CTD measurements to be a typical convection depth).

For estimating the convection depth we use the fact that at the bottom of the convective layer a step in temperature occurs (see Figure 8). The assumption is then made that in the presence of a step the inversion will ideally result in smoothed representation of the step, having half the amplitude of the step at the depth where the step actually occurs. This behavior is qualitatively confirmed in the few cases where direct comparisons are available (see Figure 5). Knowing the typical size of the deep step then, here 0.06°C above the 12.78°C of the deep water, the depth where the inversion takes half that value, i.e., $12.78^\circ + 0.03^\circ\text{C}$, should be the depth of the step itself.

This analysis has been applied to the inversions in the above three directions from the center. For T6-T2, since only 70% of the section is occupied by convected water right after the convection (Figure 9), only 70% of the volume sampled will show this step. In the range average the step will be accordingly smaller, and therefore for T6-T2 the criterion employed was to search for a temperature of $12.78^\circ + (0.7 \times 0.03^\circ\text{C}) = 12.801^\circ\text{C}$ (thus only valid in the first week or so after convection). Figure 10 shows the estimated range-averaged depth of the 12.81°C (12.801°C) isotherm, as a function of time. Here we only wish to make use of the depths found right after the convection activity, without interpreting the full time behavior. For validating the estimates, however, the depth of the 12.81°C isotherm calculated from simultaneous CTD profiles between the moorings used is also marked at various times for comparison.

The area-averaged convection depths thus found (depth of the isotherm just after the convection) are in the 1400–1600 m range, in agreement with the isolated observation we have from the hydrographic data. The latter had shown scattered depths from 800 to 1700 m, with the deeper values occurring in the center of the convection patch. Thus the results from tomography appear to be sensible, based on the other information we have about the convection depth and based on the test examples in Figure 5. This implies that smooth functions can indeed provide the convection depth and that in T6-T3, the a priori information provided through the EOF modes is able to extrapolate from data above 1000 m to the

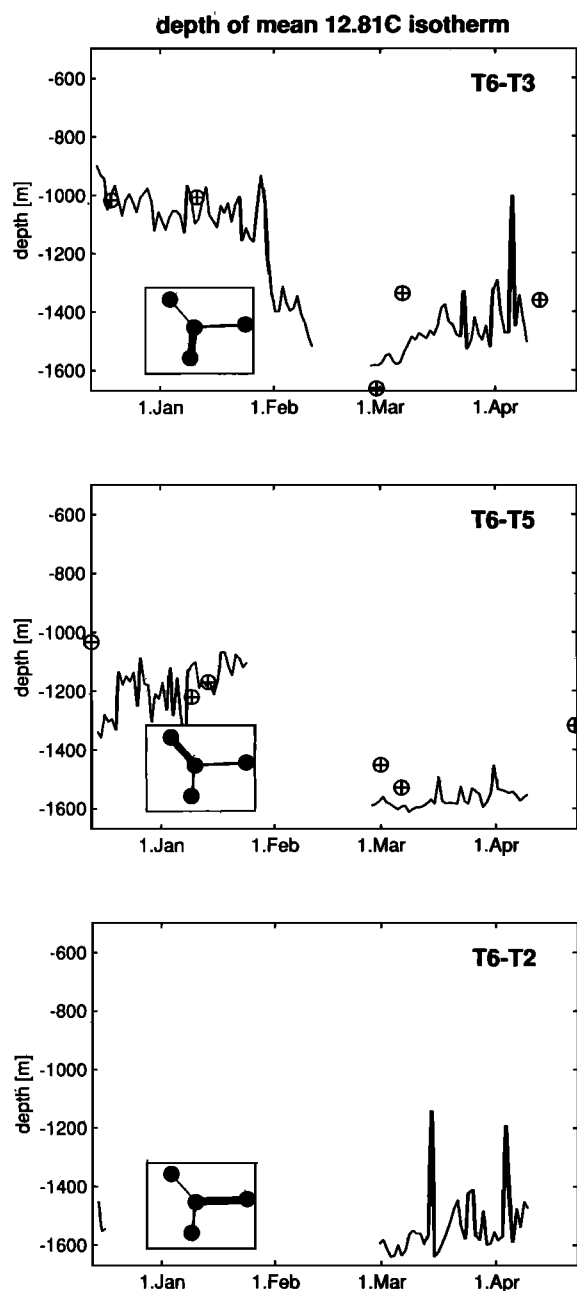


Figure 10. Estimation of the range-averaged convection depth by extracting the depth of the (top, middle) $12.78^{\circ} + .03^{\circ}$ or the (bottom) $12.78^{\circ} + .021^{\circ}$ isotherm from the tomography inversions. For comparison, the depth of the same isotherm from CTD data is indicated, whenever 2 or more CTD stations were available between the moorings considered (not done between T6 and T2, because of only partial coverage by convection).

convection depth. For T6-T5 and T6-T2 the sampling is deep enough to sense the obtained convection depth shown in Figure 10. (It should be emphasized that the information which entered from the CTD profiles via the EOFs does not simply default to the step at 1500 m when the upper and intermediate layers are unstratified, as one reviewer had suspected. The CTD profiles which determined the EOFs showed convection depths covering the entire range of 800–1700 m. Also, for T6-T5 the ray sampling was deep

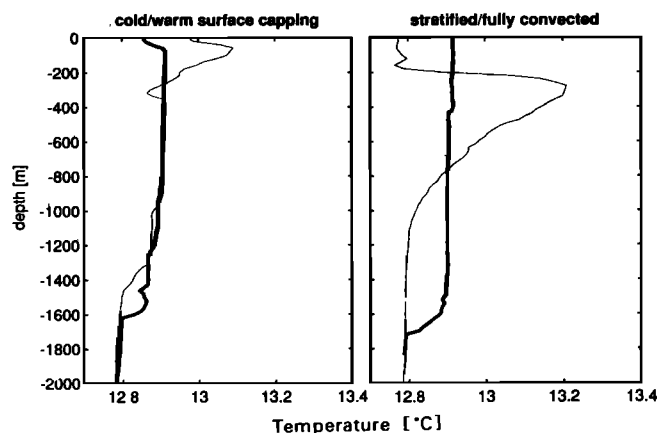


Figure 11. (left) Two profiles showing cold (heavy line) and warm (thin line) surface capping over typical convected profiles. (right) Typical pure convection and stratified profiles for comparison.

enough (1500 m) to detect shallower convection depths, if this had been the case, so the resulting 1500 m is an actual measurement. Finally, it was verified that the inversions were able to generate (smoothed) steps at depths other than 1500 m, and this causes the shoaling in T6-T3 during March and April.)

6.4. Restratification

6.4.1. Surface capping. Our CTD observations show that within a few days after the convection episode, a shallow layer ($O(50\text{--}100\text{ m})$) of less dense water starts to cap the convection patch. Mostly, the initial shallowest such layer consists of water colder (and fresher) than that generated during convection. Figure 11 shows a typical example. In addition, or afterward, light warm water will also appear in the upper 100 m or so. Such a case is included in Figure 11 as well. While both effects are active, the warm water seems to be the stronger signal in the long run (after one week), dominating below about 50 m depth. Since the shallowest tomography rays average over the upper 150 m, they are more sensitive to this warm-water capping.

The part of Figures 7a and 7b after the convection event (end of February) shows the temperature evolution of the surface layer during this phase, as derived from the tomography range average. A temperature of close to 12.9°C (indicated in Figures 7a and 7b) would be observed if the water column was still homogenized to the convection depth (based on CTD and mooring data). The mixed-layer run which was also included in Figure 7 is close to these temperatures known to be present after convection, which gives some credibility to the mixed-layer model (and to the heat fluxes used, assuming no mean advection).

The tomography inversions in Figure 7 show that in the south (T6-T3) the region is covered with a warmer than expected layer within a few days after the convection. To the northwest (T6-T5), it takes little more than 1 week for high temperatures to appear in the upper 150 m. Even before that, however, a cap of lower-density water (with temperatures still typical of convection) probably was present there, since all our CTD/XCTD profiles collected in the T6-T5 area at that time show the presence of near-surface lower-salinity water. The warm surface temperatures seen in the tomogra-

phy averages are around 13° – 13.05°C which are the highest mean 0–150 m temperatures observed in all our CTD and XCTD data. This implies that the entire region between the moorings had been capped with warm (less dense) water. The mixed-layer model remains close to the 12.9° during this warm episode, which shows that the surface layer warming is not a local (surface heating) effect, but of an advective nature (unfortunately, the ADCP data could not resolve velocity signals this close to the surface). The same data for T6-T2 (not shown) are less conclusive, since the water remained colder on average (12.95°), which is due to the cold surface layer outside the convection patch (included in this ray path).

Once the shallow lense of warm water has moved in over the patch, a gradual cooling is observed in Figures 7a and 7b until the temperatures are closer to the model prediction again. This could imply that the dense cold surface water, which was formed after convection, has returned again after temporary advection out of the region. The alternative interpretation is that the lower-density surface capping persists, but with gradually lower salinities (and temperatures). The latter view is considered more likely, since after beginning of March, no CTD/XCTD profiles without low-density surface capping were found anywhere, and since a return of high-density surface water would be inconsistent with the underlying return of warm LIW water (see next section), at least for T6-T3.

From about mid-March the surface layer temperatures observed with the tomography follow the mixed-layer model prediction again, through the cooling event at the end of March. That cooling is sufficiently strong to erase the new surface stratification that has been built up. In the tomography inverses it causes partial cooling also at the LIW level (see Figure 9). In the model run the event penetrates to large depths, since the model cannot reproduce the warming LIW layer below (see next section), but remains unstratified there. After this cooling a new warm cap appears.

6.4.2. LIW restratification. The return of LIW water can be followed in an integral sense in Figure 9. We see that after the convection phase which had homogenized the water column, the stratified water at the LIW level gradually returns in the south (T6-T3) and in the east (T6-T2). By contrast, in the T6-T5 section, the convected water remains in place for the whole sampling period. In the T6-T5 section, only a very slow warming/return of LIW water is visible. These different trends are confirmed by the CTD observations during the recovery cruise in April (see Figure 6). At that time, rather homogeneous profiles (below the surface layer) were still found between T5 and T6, while T6-T3 had significantly restratified.

The warming at this level is not continuous. There are two episodes of intermediate cooling, one in mid-March, and a stronger one near the end of March. The second one is quite clearly related to the atmospheric cooling discussed in the previous section, where the heat loss was strong enough to cool the layer below 150 m as well. The earlier cooling is pronounced only at T6-T2 and must be due to some cold advection. The restratification rates before and after these intermediate cooling phases have been estimated from the straight-line fits indicated in Figure 9. Translated into temperatures, the corresponding increase is $0.8^{\circ} \pm 0.2 \times 10^{-2}^{\circ}\text{C}$ per day. Since the first cooling at T6-T2 has an advective

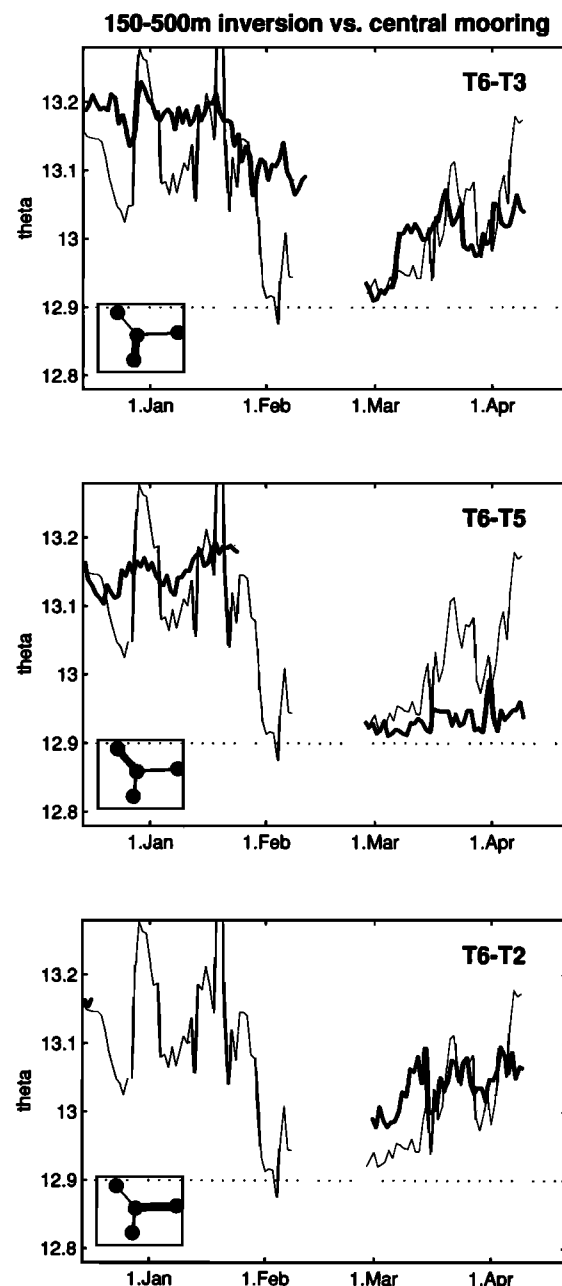


Figure 12. Temperature evolution of the Levantine Intermediate Water (LIW) 150–500 m layer in the three main directions from the central mooring, compared to the same quantity estimated from the central mooring T6.

nature, one cannot exclude that this is part of the restratification process (e.g., through eddy activity). Therefore a rate has also been estimated including this cooling, up to the leveling off resulting from the second atmospheric cooling (indicated as a dashed line). This rate is $0.5 \times 10^{-2}^{\circ}\text{C}$ per day, and thus nearly within the above range. At these observed restratification rates it would take about 40 days ($\pm 30\%$) to reestablish the preconvection conditions in the LIW layer.

Figure 12 shows the temperature equivalent of Figure 9 but now plotted together with the central T6 mooring estimates of the 150–500 m layer temperature. Comparison of the range averages with the central mooring data shows that

the warm water appears from the south and the east, since for those directions the warming starts in the range average, but not at the center. Once it reaches the central mooring, the temperature rise there is larger than in the tomography average during both warming events seen there. The only explanation for such an evolution is that the warming arrives at T6 in the form of a localized eddy or meander with higher LIW temperatures at that place than along the three directions sampled.

7. Discussion and Conclusions

The tomography data have proven to be an ideal complement to moored and CTD observations. While moored temperature and current observations are a good means to document the evolution of the convection regime at a point, the tomography observations add information about the evolving spatial extent and the larger-scale properties of the system. The CTD data helped to illustrate the detailed vertical structures during a few phases of the development. In particular, we were fortunate to be present in the area during the main convection activity and get close-up looks of the various convection profiles. At the same time, the CTD provided comparison/initialization data for the tomography inversions. It is worthwhile to note, however, that much of the information about the system, in particular the extent of the convection region, could have been obtained from the tomography time series alone.

It was shown with the tomography data that on the convection-patch scale, the heat content evolution of the water column generally followed the integral of the surface heat fluxes, from the seasonal cooling during December and January all the way through to the convection period in mid-February. Such agreement on the large scale is a stronger result than comparison at a single mooring can give, since absence of advection in the whole region indicates that the water had been confined to the area of strongest cooling for a significant amount of time. This result was quantified, based on the degree of agreement and the uncertainty in the heat fluxes. It could be shown, that no permanent exchange with the surrounding more strongly stratified 0–500 m layer had occurred during the 2 months leading up to the convection. This means that the water had been trapped in the region by the local circulation and thus was subject to the heat fluxes for the months before the convection. This would set the convection patch size even without strongly localized surface buoyancy fluxes. It suggests that an important factor in determining the size and location of the convection is this confinement of water through the circulation.

The surface layer can be better observed with the surface-trapped acoustic propagation than with subsurface moorings. Comparison of the tomography inversions with mixed-layer calculations shows good agreement, including the warming due to entrainment of the Levantine Intermediate Water. At the same time, the spatial extent of this process could be observed and was in agreement with the later CTD data from the convection cruise.

The individual CTD stations occupied with the ship showed a high degree of spatial variability of convection strength, depth, presence, and in the vertical property distributions (see Figure 5). The tomography inversions are able to average over these highly variable distributions, as demonstrated in Figure 5. Thus the inversions have provided

an integrated estimate for the amount of convected water in the convection patch and also for the mean convection depth. The results imply a volume of approximately 60 km radius occupied by convection, the mean convection depth being 1500 m. These numbers are consistent with the area and depth range in which CTD stations showed homogenized water. The resulting 0.3 Sv of annual-mean new water formation agree with currently accepted values for formation rates of Western Mediterranean Deep Water.

A current question of interest is how the convected water escapes from the deep-mixed regime, or how the stratified water moves back in. Combined CTD and tomography observations show that within a few days, a light thin surface lense moves in over the region. The temperature of this capping layer was somewhat variable, and a strong cooling event about 1 month after the convection removed the surface stratification again temporarily (while the restratifying LIW layer was only partly affected).

The restratification at the LIW level is distinctly different from that in the surface layer. The inversions for the amount of LIW have shown that the dense water in the southern and eastern part of the convection patch is removed on a 40-day timescale. The corresponding warming rate derived implies a flux of 0.3 Sv°C into the convection patch, assuming a volume of 60 km radius and 350 m depth for the LIW. If horizontal eddy transports $\overline{u'T'}$ were responsible for this flux as in patch breakup by baroclinic instability [Gascard, 1978; Send and Marshall, 1995], the corresponding u' could be estimated from this, using $\pi R^2 h \Delta T / 40^d = 2\pi R h \overline{u'T'} \approx \pi R h u' \Delta T$. This gives $u' = R/40^e = 1.7 \text{ cm s}^{-1}$ required for motions that exchange water with the surroundings. Our moorings give typically 2–8 cm s^{−1} for the overall rms eddying motions at 250–300 m depth, showing that the expected order of magnitude for u' is feasible.

The restratification observed, however, does not seem to occur in the northwestern part of the convection region. In that area a remnant of the convection patch of 50–60 km diameter persists until the end of the experiment, though covered by a near-surface cap of light water as well. This might be related to increased stability of the boundary because of the topography or strong coastal currents there. Along the connecting lines of T6-T3 and T6-T2, where restratification occurs, some information about the spatial structure of the returning LIW is available. The advection at these levels moves in from the south and east. It appears to reach the center as a local maximum in temperature. A possible distribution consistent with this is sketched in Figure 13. It is very suggestive of the meandering that is known to exist from earlier observations and numerical model simulations, which results from baroclinic instability of the convection patch. In the present case this seems to act to reduce the diameter of the patch by one half over the course of the experiment.

Appendix A: Surface Heat Flux Calibration

All terms contributing to the surface heat flux in the Peridot model were found to have significant biases. The model long-wave back radiation had an average value of 97 W m^{−2} during the 90 days analyzed. Using the standard bulk formulae with the observed water and air temperatures, however, and estimating the cloud fraction from the Peridot insolation values, an average of 65 W m^{−2} was obtained.

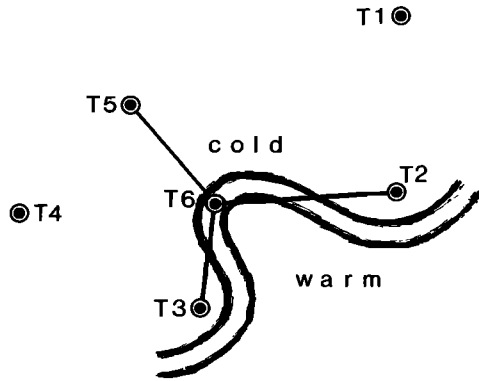


Figure 13. Sketch of a LIW layer temperature structure consistent with the tomography and mooring observations.

This value is much more realistic, since even the clear-sky values for our water temperature and wet/dry air temperatures give only 80 W m^{-2} . The resulting correction of -32 W m^{-2} for the long-wave radiation is the same that results from the comparison of Peridot long-wave fluxes with other sources [e.g., Garrett et al., 1993], when averaged over the whole basin and over an annual cycle [Martel and Martel, 1994].

The clear-sky insolation, however, is underestimated in the Peridot model. A difference of 17 W m^{-2} exists to the widely used parameterization by Lumb [1964]. Our direct shipboard observations of this flux from two cruises suggest even slightly higher maximum values. Therefore we adopt a correction of $+20 \text{ W m}^{-2}$ for the Peridot short-wave flux.

The largest error is present in the latent heat flux. This is due to an underestimate of the wind speed, as could be verified by comparing Peridot winds with our shipboard observations. Two independent tests suggest that as a result the latent heat flux is too small in the model by about 40 W m^{-2} . The first came from calibrating coastal meteorological observations with a total of 8 months of observations on a moored platform in this region during the winters of 1976 and 1977 [Mertens, 1994]. The least squares fit used there had produced land-based estimates for wind speed and thus latent heat fluxes that were too low in the mean, the latter by 40 W m^{-2} . Application of the same formula to our winter of 1991–1992, however, yielded agreement of land-based and Peridot latent heat fluxes to within 3 W m^{-2} . This suggested that the winter-mean Peridot latent flux was also too low by 40 W m^{-2} . In addition, the 3 weeks of observations during our *Poseidon* cruise also yielded a difference in 40 W m^{-2} to the Peridot model. Since this offset is further in agreement with the annual and basin-mean comparison by Martel and Martel [1994], we adopt a linear correction to the wind speed and thus to the latent heat flux by the factor which increases the mean latent heat flux by 40 W m^{-2} . This is a factor of 1.37.

The correction factor for wind speed likewise increases the sensible heat flux by the same factor, resulting in a mean correction of 8 W m^{-2} . This agrees to within 5 W m^{-2} with the difference of Peridot to both *Poseidon* and the land-based estimates. Thus a correction by a factor of 1.37 is consistent both with the latent flux error and the shipboard data.

All of these corrections are well established through either identical results of other studies on independent time/space

scales or by direct observations in the area during the time of interest. The remarkable net result of the various adjustments is that the total heat budget of the Peridot surface fluxes is changed by only 10 W m^{-2} .

Appendix B: Inversion Error Estimates

The inversion errors for the sound speed estimate $\hat{c}(z)$ can be estimated from the inverses as

$$\langle [c(z) - \hat{c}(z)]^2 \rangle = \mathbf{p}(z) \mathbf{H} \mathbf{p}(z)^T \quad (2)$$

where \mathbf{H} is the error covariance matrix for the inverse estimate

$$\mathbf{H} = (\mathbf{I} - \mathbf{R}) \mathbf{W} (\mathbf{I} - \mathbf{R})^T + \mathbf{G}^{-g} \mathbf{E} \mathbf{G}^{-gT} \quad (3)$$

$\mathbf{R} = \mathbf{G}^{-g} \mathbf{G}$ being the resolution matrix, $\mathbf{p}(z)$ is a row vector with the modal shape values at depth z , and \mathbf{I} is the identity matrix. Writing all the modal shapes as a matrix \mathbf{P} containing different depths down a column and the different modes along the rows, an expression for the vector with the error at each depth is

$$\langle [c - \hat{c}]^2 \rangle = \text{diag}(\mathbf{P} \mathbf{H} \mathbf{P}^T). \quad (4)$$

The size of the inversion errors thus estimated have been included in Figure 5. It had also been verified by carrying out simulations for the inverses, using actual CTD profiles to theoretically predict the acoustic arrivals. After adding realistic measurement noise a number of ray arrivals were used to invert back for the initial CTD profile. The inverse results were found to always lie within the error estimate of the used profile. Simulations like this had also been used in the design of the experiment.

For the layer averages the error can be estimated as

$$\begin{aligned} & \left\langle \left[\frac{1}{H} \int c dz - \frac{1}{H} \int \hat{c} dz \right]^2 \right\rangle \\ &= \frac{1}{H^2} \sum_i \sum_j H_{ij} \iint \mathbf{p}_i(z) \mathbf{p}_j(z') dz dz' \end{aligned} \quad (5)$$

where H is the depth of the layer averaged over. Note that the double integral needs to be evaluated only once in this representation.

Acknowledgments. This project was only made possible through the contributions from a large number of people, by participating in the cruises and their preparation, by taking care of the instruments, and by helping with the data analysis. Particular mention is owed to G. Krahmann, J. Fischer, L. Stramma, M. Visbeck, H. Treede, U. Papenburg, T. Terre, and F. Evannou. The cooperation of C. Mertens by providing mixed-layer model runs and general assistance is gratefully acknowledged. The project as a whole was enriched by the participation of our partners from FORTH/IACM Crete. The experiment and project was made possible by funding from the European Community MAST program (contract MAST 0008-C), the German Ministry of Science and Technology (BMFT contract 03F0542A), and the Programme Atmosphère Météorologique et Océan Superficiel (CNRS).

References

- Aki, K., and P. Richards, *Quantitative Seismology, Theory and Methods*, vols. 1 and 2, W. H. Freeman, New York, 1980.
- Bryden, H. L., and T. H. Kinder, Steady two-layer exchange

- through the Strait of Gibraltar, *Deep Sea Res.*, **38**, suppl., 445–463, 1991.
- Bryden, H. L., and H. M. Stommel, Origin of the Mediterranean outflow, *J. Mar. Res.*, **40**, suppl., 55–71, 1982.
- Garrett, C., R. Outerbridge, and K. Thompson, Interannual variability in Mediterranean heat and buoyancy fluxes, *J. Clim.*, **6**, 900–910, 1993.
- Gascard, J.-C., Mediterranean deep water formation baroclinic instability and oceanic eddies, *Oceanol. Acta*, **1**, 315–330, 1978.
- Jones, H., and J. Marshall, Convection with rotation in a neutral ocean, *J. Phys. Oceanogr.*, **23**, 1009–1039, 1993.
- Lumb, F. E., The influence of cloud on hourly amounts of total solar radiation at the sea surface, *Q. J. R. Meteorol. Soc.*, **90**, 43–56, 1964.
- Martel, L., and F. Martel, Air-sea fluxes and winds over the western Mediterranean Sea from three sets: FNOC, Peridot 1988–1989, Peridot 1991–1992, technical report, Euromodel/CETIIS, Ivry sur Seine, France, 1994.
- MEDOC Group, Observation of formation of deep water in the Mediterranean, *Nature*, **227**, 1037–1040, 1970.
- Mertens, C., Winterliche deckschichtentwicklung und ihre zwischenjährliche variabilität im nordwestlichen Mittelmeer, (in German), diploma thesis, Univ. of Kiel, Kiel, Germany, 1994.
- Munk, W. H., and C. Wunsch, Ocean acoustic tomography: A scheme for large scale monitoring, *Deep Sea Res.*, Part A, **26**, 123–161, 1949.
- Rhein, M., Deep water formation in the western Mediterranean, *J. Geophys. Res.*, this issue, 1995.
- Schott, F., and K. D. Leaman, Observations with moored acoustic doppler current profilers in the convection regime in the Golfe du Lion, *J. Phys. Oceanogr.*, **21**, 558–574, 1991.
- Schott, F., M. Visbeck, and U. Send, Open ocean deep convection, Mediterranean and Greenland Seas, in *Ocean processes in Climate Dynamics*, edited by P. Malanotte-Rizzoli and A. Robinson, pp. 203–225 Kluwer Academic, Norwell, Mass., 1994.
- Send, U., and J. Marshall, Integral effects of deep convection, *J. Phys. Oceanogr.*, in press, 1995.
- Spiesberger, J., Ocean acoustic tomography. Travel time biases, *J. Acoust. Soc. Am.*, **77**, 83–100, 1985.
- Spiesberger, J., and P. Worcester, Perturbations in travel time and ray geometry due to mesoscale disturbances: A comparison of exact and approximate solutions, *J. Acoust. Soc. Am.*, **74**, 219–225, 1983.
- Spindel, R. C., Signal processing in ocean tomography, in *Adaptive Methods in Underwater Acoustics*, edited by H. G. Urban, pp. 687–710, D. Reidel, Norwell, Mass., 1985.
- THETIS Group, Open-ocean deep convection explored in the Mediterranean, *Eos Trans. AGU*, **75**, 217–221, 1994.
- Worcester, P. F., et al., Evolution of the large-scale temperature field in the Greenland Sea during 1988–89 from tomographic measurements, *Geophys. Res. Lett.*, **20**, 2211–2214, 1993.
- Y. Desaubies and F. Gaillard, Laboratoire de Physique des Océans, IFREMER, BP 70, 29280 Plouzané, France.
- F. Schott and U. Send, Düsternbrooker Weg 20, 24105 Kiel, Germany. (e-mail: usend@ifm.uni-kiel.d400.de)

(Received May 26, 1994; revised October 13, 1994; accepted November 15, 1994.)